optica

Coupled ptychography and tomography algorithm improves reconstruction of experimental data

MAIK KAHNT[1,2,*], JOHANNES BECHER[5], DENNIS BRÜCKNER[1,2,3], YAKUB FAM[5], THOMAS SHEPPARD[4,5], TOBIAS WEISSENBERGER[6], FELIX WITTWER[1,2], JAN-DIERK GRUNWALDT[4,5], WILHELM SCHWIEGER[6], AND CHRISTIAN G. SCHROER[1,2]

[1] *Deutsches Elektronen-Synchrotron DESY, Notkestraße 85, 22607 Hamburg, Germany*
[2] *Department Physik, Universität Hamburg, Luruper Chaussee 149, 22761 Hamburg, Germany*
[3] *Ruhr-University Bochum, Faculty of Chemistry and Biochemistry, Universitätsstr. 150, 44801 Bochum, Germany*
[4] *Institute of Catalysis Research and Technology, Karlsruhe Institute of Technology, Hermann-von-Helmholtz Platz 1, 76344 Eggenstein-Leopoldshafen, Germany*
[5] *Institute for Chemical Technology and Polymer Chemistry, Karlsruhe Institute of Technology, Engesserstr. 20, 76131 Karlsruhe, Germany*
[6] *Institute of Chemical Reaction Engineering, Friedrich-Alexander-University Erlangen-Nürnberg, Egerlandstraße. 3, 91058 Erlangen, Germany*

[*] *Corresponding author: maik.kahnt@desy.de*

Published 26 September 2019

This document provides supplementary information to "Coupled ptychography and tomography algorithm improves reconstruction of experimental data," https://doi.org/10.1364/OPTICA.6.001282. Three-dimensional X-ray microscopy by ptychographic tomography requires elaborate numerical reconstructions. We describe a coupled ptychography-tomography reconstruction algorithm and apply it to an experimental ptychographic X-ray computed tomography data set of a catalyst particle. Compared to the traditional sequential algorithm, in which ptychographic projections are reconstructed to serve as input for subsequent tomographic reconstruction, the coupled ptychography-tomography algorithm reconstructs the 3D volume with higher spatial resolution over a larger field of view. Coupling the data from different projections improves the overall reconstruction, and the ptychographic sampling in individual projections can be coarsened beyond the point of overlap between neighboring scan points, still leading to stable reconstructions.

1. SAMPLE SYNTHETIZATION

The hierarchical TS-1 zeolite sample was synthesized by using mesoporous, spherical silica particles as sacrificial template for the macropore formation [1, 2]. In a typical synthesis, 1 g of calcined mesoporous, spherical silica particles (MSPs) were impregnated with 1.38 g of a 40.0 wt.-% aqueous tetrapropylammonium hydroxide solution. The impregnated MSPs were then dried at 313 K and the dry powder was transferred into a PTFE crucible. The zeolite synthesis was carried out by steam-assisted crystallization (SAC) at 423 K for 48 h. After crystallization, the solid product was recovered by filtration and dried at 348 K for 12 h. To remove the structure directing agent, the sample was calcined under 300 l/h air flow for 6 hours at 823 K (heating ramp 1.2 K/min).

2. PXCT AND CPT RECONSTRUCTIONS

projection alignment

The alignment of the 90 projections $O_\Theta(\vec{\rho})$, reconstructed using the ePIE algorithm, was performed using only the phase information. The phase images were cropped to include only the particle, a bit of air and the beginning of the platinum podium in the field of view (FOV). The part of the podium which created

phase wraps was cropped out of the FOV leaving only non-phase wrapping features in it. Moreover, the cropping was chosen in a way that the left and right edge of the field of view were only air from the top all the way to the bottom. Afterwards the phase wedge in the background was removed independently for each projection by taking the air to the left, to the right and above the sample as a reference. The first alignment step was purely in vertical direction. To this end the vertical profiles $p_{\Theta,v}\left(\rho_y\right)$ of the $O_\Theta\left(\vec{\rho}\right)$ were calculated as the horizontal line integrals:

$$p_{\Theta,v}\left(\rho_y\right) = \int O_\Theta\left(\vec{\rho}\right)\,\mathrm{d}\rho_x \tag{S1}$$

The derivative of all vertical profiles $p_{\Theta,v}$ were correlated to the first profile in the list.

The estimated shifts $\Delta\rho_y\left(\Theta\right)$ (with sub-pixel precision) were applied to the original uncropped projection $O_\Theta\left(\vec{\rho}\right)$ and saved. Then the cropping and the phase-wedge removal were repeated as described above, as new features might have entered he field of view or other features might have left the field of view. The second alignment step was performed in the horizontal direction. The horizontal profiles $p_{\Theta,h}\left(\rho_x\right)$ of the $O_\Theta\left(\vec{\rho}\right)$ were calculated as the horizontal line integrals:

$$p_{\Theta,h}\left(\rho_x\right) = \int O_\Theta\left(\vec{\rho}\right)\,\mathrm{d}\rho_y \tag{S2}$$

Possible offsets of the horizontal profiles $p_{\Theta,h}$ were removed by taking the far left and far right of the profiles as zero reference. Then the center of mass of each horizontal profile was calculated and the shifts $\Delta\rho_x\left(\Theta\right)$ needed to align the center of mass with the horizontal center of the field of view were calculated.

The horizontal and vertical shifts were then applied to the original uncropped projection $O_\Theta\left(\vec{\rho}\right)$. The cropping and removal of phase wedges was repeated. And the vertical alignment was repeated and the estimated additional shifts were added to the already saved ones. This cycle was repeated in an alternating fashion for vertical and horizontal alignment, each time adding the newly estimated shifts to the saved ones, shifting the original projections, cropping them and freeing them from phase wedges. Always shifting the original projections prevented the smoothing over time, when appling sub-pixel shifts every iteration.

During this circle the cropping was twice changed to a slightly smaller field of view as the coarse alignment was already advanced. After 6 iterations of vertical and horizontal alignment no further refinement to the shifts were calculated. The alignment step was stopped and the resulting shifts were applied to the original projections.

A. Description of the CPT algorithm

The starting point is a guess of the complex-valued three-dimensional volume $n\left(\boldsymbol{r}\right)$. In this case the non-absorbing and non-phase shifting empty sample was chosen as the first guess. Moreover, the volume was not kept as a matrix with complex entries, but separated into a phase shift volume $\Phi\left(\boldsymbol{r}\right)$ and the logarithmic modulus volume $A\left(\boldsymbol{r}\right)$ to allow dealing with the amplitude in a simpler way later on.

$$A\left(\boldsymbol{r}\right) = -k\cdot\beta\left(\boldsymbol{r}\right) \tag{S3}$$

$$\Phi\left(\boldsymbol{r}\right) = k\cdot\delta\left(\boldsymbol{r}\right) \tag{S4}$$

$A\left(\boldsymbol{r}\right)$ and $\Phi\left(\boldsymbol{r}\right)$ are the products of the wave number k with $\beta\left(\boldsymbol{r}\right)$ and $\delta\left(\boldsymbol{r}\right)$ [see Eqn. (4)]. Starting with one randomly chosen

Algorithm S1. Coupled ptychography and tomography reconstruction of a PXCT dataset. This algorithm equals the framework of [3] with M iterations of the ePIE algorithm [4] used as data constraint and the SART algorithm for the object constraint.

procedure PTYCHOTOMO($I_u, \varrho_{\Theta,k}, P_\Theta\left(\rho_x,\rho_y\right)$)
  create a 3D array $A\left(\boldsymbol{r}\right)$ for the logarithmic modulus and a 3D array $\Phi\left(\boldsymbol{r}\right)$ for the phase shift. ▷ initial entries 0
  if no $P_\Theta\left(\rho_x,\rho_y\right)$ are given **then**
    initialize appropriate $P_\Theta\left(\rho_x,\rho_y\right)$ for each recorded projection angle Θ
  loop N times
    for every Θ **do**
      calculate the projections $a_\Theta\left(\rho_x,\rho_y\right)$ and $\phi_\Theta\left(\rho_x,\rho_y\right)$ under the angle Θ
      calculate the complex projection $O_\Theta\left(\rho_x,\rho_y\right) = \exp a_\Theta\left(\rho_x,\rho_y\right)\cdot\exp\left(\mathrm{i}\phi_\Theta\left(\rho_x,\rho_y\right)\right)$
      do M ptychography iterations on $O_\Theta\left(\rho_x,\rho_y\right)$ using $I_{\Theta,j}\left(u\right)$, $\varrho_{\Theta,j}$ and P_Θ to obtain an updated guess $\hat{O}_\Theta\left(\rho_x,\rho_y\right)$ for that projection ▷ e. g., using the ePIE algorithm
      calculate the logarithmic modulus $\Delta a_\Theta\left(\rho_x,\rho_y\right) = \log\left|\hat{O}_\Theta\left(\rho_x,\rho_y\right)\right| - \log\left|O_\Theta\left(\rho_x,\rho_y\right)\right|$ and phase shift update $\Delta\phi_\Theta\left(\rho_x,\rho_y\right) = \arg\left(\hat{O}_\Theta\left(\rho_x,\rho_y\right)\right) - \arg\left(O_\Theta\left(\rho_x,\rho_y\right)\right)$
      calculate the 3D logarithmic modulus and phase shift updates $\Delta A_\Theta\left(\boldsymbol{r}\right)$ and $\Delta\Phi_\Theta\left(\boldsymbol{r}\right)$ by back-projecting $\Delta a_\Theta\left(\rho_x,\rho_y\right)$ and $\Delta\phi_\Theta\left(\rho_x,\rho_y\right)$ under the angle Θ
      update the object volumes: $A\left(\boldsymbol{r}\right) \leftarrow A\left(\boldsymbol{r}\right) + \gamma\cdot\Delta A_\Theta\left(\boldsymbol{r}\right)$ and $\Phi\left(\boldsymbol{r}\right) \leftarrow \Phi\left(\boldsymbol{r}\right) + \gamma\cdot\Delta\Phi_\Theta\left(\boldsymbol{r}\right)$ ▷ update strength $\gamma\in(0,1]$
  return $A\left(\boldsymbol{r}\right)$ and $\Phi\left(\boldsymbol{r}\right)$

rotation angle Θ, the 2D projections $a_\Theta\left(\rho_x,\rho_y\right)$ and $\phi_\Theta\left(\rho_x,\rho_y\right)$ are calculated according to:

$$a_\Theta\left(\rho_x,\rho_y\right) = \int_{-\infty}^{+\infty} A\left(\mathbf{R}_\Theta\boldsymbol{\rho}\right)\,\mathrm{d}\rho_z \tag{S5}$$

$$\phi_\Theta\left(\rho_x,\rho_y\right) = \int_{-\infty}^{+\infty} \Phi\left(\mathbf{R}_\Theta\boldsymbol{\rho}\right)\,\mathrm{d}\rho_z \tag{S6}$$

The complex valued two-dimensional projection $O_\Theta\left(\rho_x,\rho_y\right) = \exp\left(a_\Theta\left(\rho_x,\rho_y\right) + \mathrm{i}\phi_\Theta\left(\rho_x,\rho_y\right)\right)$ is used as initial object for M iterations of the ePIE algorithm [4]. This algorithm uses the diffraction patterns $I_{\Theta,j}\left(q_x,q_y\right)$, the corresponding positions $\boldsymbol{\varrho}_{\Theta,j}$, and the 2D probe functions $P_\Theta\left(\rho_x,\rho_y\right)$ for the given projection angle Θ. Performing M iterations of the ePIE algorithm results in an updated 2D probe function, which is kept and replaces its previous estimate, and the updated estimate for the complex 2D projection $\hat{O}_\Theta\left(\rho_x,\rho_y\right)$. To project the difference between the initial guess $O_\Theta\left(\rho_x,\rho_y\right)$ and $\hat{O}_\Theta\left(\rho_x,\rho_y\right)$ back to the 3D volume, the logarithmic modulus and phase shift (real and imaginary part) are separated again:

$$\Delta a_\Theta\left(\rho_x,\rho_y\right) = \log\left|\hat{O}_\Theta\left(\rho_x,\rho_y\right)\right| - \log\left|O_\Theta\left(\rho_x,\rho_y\right)\right| \tag{S7}$$

$$\Delta\phi_\Theta\left(\rho_x,\rho_y\right) = \arg\left(\hat{O}_\Theta\left(\rho_x,\rho_y\right)\right) - \arg\left(O_\Theta\left(\rho_x,\rho_y\right)\right) \tag{S8}$$

To update the 3D volume for $A(\boldsymbol{r})$ and $\Phi(\boldsymbol{r})$, the 2D updates $\Delta a_\Theta(\rho_x, \rho_y)$ and $\Delta\phi_\Theta(\rho_x, \rho_y)$ are back projected under the projection angle Θ. Using these 3D back projections, the two volumes $A(\boldsymbol{r})$ and $\Phi(\boldsymbol{r})$ are updated.

This procedure of projecting the updated volume, running M iterations of ePIE and back-projecting the differences onto the volume is then performed for the next projection angle Θ. Once each of the recorded projection angles Θ was used this way, one iteration of the CPT algorithm is finished. The next iterations are done in exactly the same way, now using the newly updated estimates for the object volumes $A(\boldsymbol{r})$ and $\Phi(\boldsymbol{r})$ and the probes $P_\Theta(\rho_x, \rho_y)$. After N iterations of the previous procedure, algorithm S1 finishes.

Choice of reconstruction parameters

The parameters α and β describe the update strength of the object function and probe function during every iteration of the ePIE algorithm. Choosing values < 1 would result in the update step performing only a fraction of step that the data suggests. This would slow down the convergence of the reconstruction, but would further stabilize the iterative algorithm. As the probe function was initialized with a good estimate, the algorithm converged reliably with maximal update strength. Therefore, $\alpha = 1$ and $\beta = 1$ were chosen, balancing speed and robustness of the convergence. The parameter γ describes the update strength for the two volumes after the ptychographic step in the CPT algorithm. Here, too, the full update strength $\gamma = 1$ led to stable and fast convergence.

The parameter M describes the number of ePIE iterations performed on a projection before updating the two volumes in the ePIE algorithm. Choosing M larger would result in more ePIE iterations being performed on a projection, effectively reducing the coupling of all projections. The more frequent the CPT algorithm switches between projections, the more frequently the information is shared between projections via the shared volumes. Choosing M very large leads to reconstructing each projection for many iterations on its own, without exchange of information with all other projections. This would bring the CPT algorithm closer to the PXCT algorithm, as it would require each projection to properly reconstruct on its own. We have chosen the parameter $M = 1$ as it provides the strongest coupling between all recorded projections.

The parameter N describes how often the CPT algorithm iterates over all projections. As with all iterative algorithms, this parameter depends on the dataset at hand. For the given dataset, we chose $N = 50$ as a compromise between convergence and computation time. In the current CPU implementation of the algorithm on a single computer, $N = 50$ iterations took about one week. At the last iteration, the updates to the reconstruction were small, suggesting near convergence. The fast convergence was aided by the use of the very good initial probe estimate.

For the proper comparison of both PXCT and CPT, we also chose 50 iterations for the ePIE algorithm for each projection in PXCT. Hence, each recorded diffraction pattern under every recorded projection angle was used exactly 50 times to update its respective projection in PXCT, while each diffraction pattern in the CPT algorithm was also used exactly 50 times to update the shared volumes. Subsequently, the SART step of the PXCT algorithm was also performed 50 times, resulting in the volumes also being updated 50 times from each recorded direction as in the CPT algorithm.

3. RESOLUTION EVALUATION

Line profiles

Floating masses were observed in some of the macro pores, proving they might not be completely empty but filled with low density and weakly scattering material. Therefore, profiles across surfaces between the bulk material and the internal macropore structure were not evaluated, only line profiles located on the border between the surrounding air and the macro-porous zeolite particle. Furthermore, the line profiles were chosen along the four major directions inside the tomographic plane. Finally each line profile was chosen in a position that allowed for at least 600 nm of air in one direction and 600 nm of sample material in the other direction to allow for a proper baseline for the fitted error function at both ends. The line profiles, their positions, and the fitted error functions are shown in Fig. S1. For all profiles the edge width in the volume reconstructed using the CPT framework was the smaller one.

Fourier shell correlation

To evaluate the resolution averaged over all directions via Fourier shell correlation (FSC), two independently recorded volumes are needed. As the sample was only measured once, the dataset was split into two halves. Separating the dataset by using every other recorded angle was not an option, as it would reduce the angular sampling and therefore worsen the achieved resolution in the tomographic plane. That is why the dataset was separated by alternating between every single diffraction pattern (see Fig. S2). This increases the effective lateral scanning step size in each dataset by a factor of $\sqrt{2}$ (still a grid scan, but 45° tilted), but did not reduce the angular sampling. This increase in effective lateral scanning step size reduces the overlap between neighboring scan positions. However, the initial step size of 400 nm for a probe size of 1800 nm was already conservative and the increased step size still leaves sufficient overlap for a successful ptychographic reconstruction (see Fig. S2b-c).

Each of the two half datasets was independently reconstructed once using the PXCT framework and once using the CPT framework. All four resulting complex-valued volumes were 660^3 voxel in size. The center 330^3 voxels were cropped out and filted with a three dimensional Hanning filter before calculating the Fourier shell correlations of the two pairs of volumes (see Fig. S3). The half-bit threshold [5] was used, as volumes reconstructed from half datasets were correlated. The resolution estimated for the CPT reconstructed volumes surpasses that of the volumes reconstructed using the PXCT framework.

Spectral signal to noise ratio

Using the calculated Fourier shell correlations, we calculated the spatial signal to noise ratio (SSNR)[6] as:

$$SSNR(q) = 2\frac{FRC(q)}{1 - FRC(q)} \tag{S9}$$

Here, as well, the volumes reconstructed using the CPT framework indicate the better resolution (see Fig. S4).

4. CPT WITH REDUCED SAMPLING

When reducing the sampling in the horizontal direction, the quality of the CPT reconstructions is also reduced. This reduction can be explained by effectively imaging the sample with a smaller dose. Moreover, a reduction in the total number of diffraction patterns means that the volumes get updated less often using

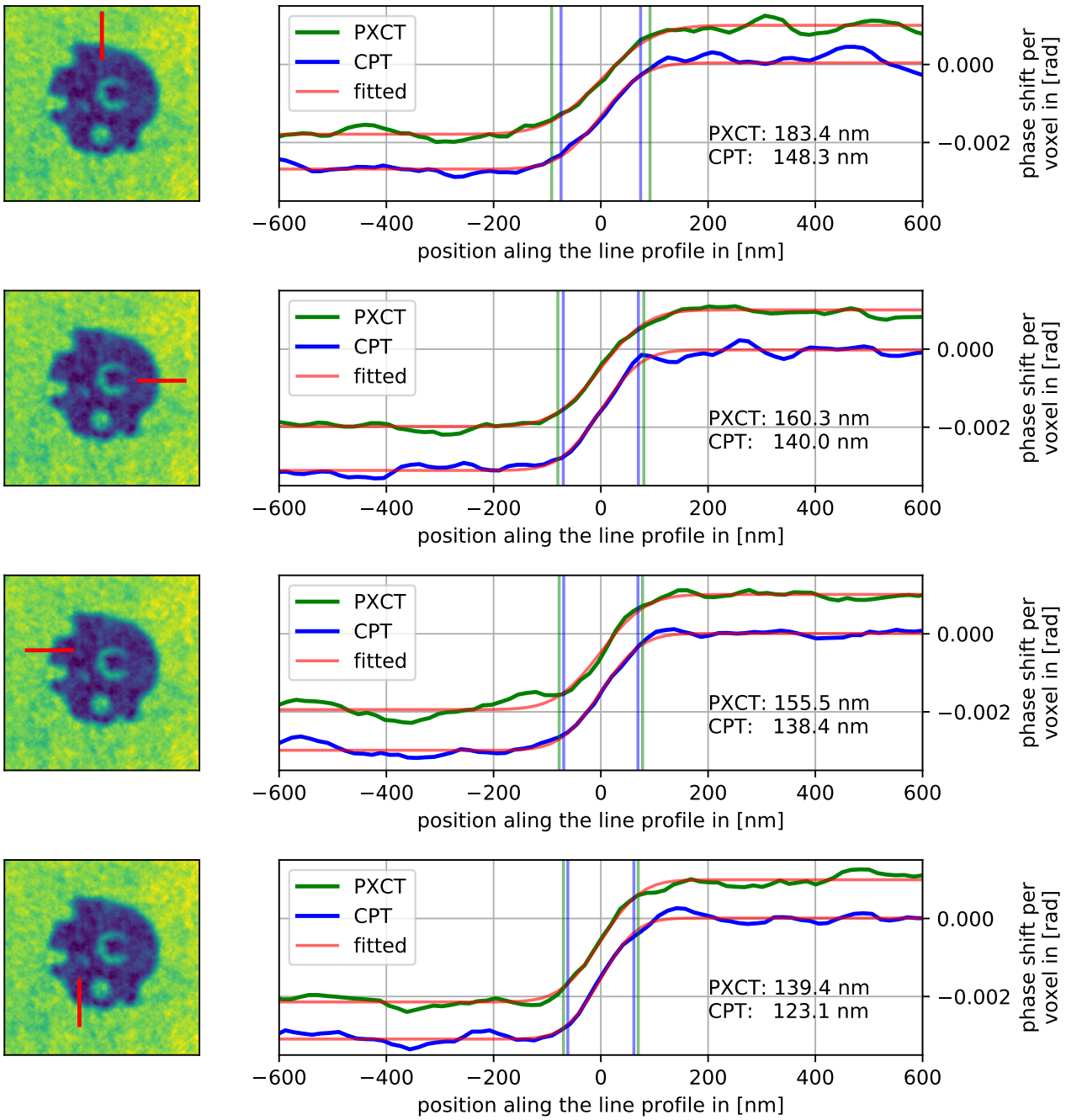

Fig. S1. Fitting of line profiles across four edges in the PXCT and CPT reconstructions of the hierarchical zeolite. Left: reconstructed slice with the position of the lines; Right: line profiles for the PXCT and CPT reconstructions together with respective error-function fits. The width of the edge is determined as the interval between the 10% and 90% level of the fits. In all cases the CPT reconstruction has a slightly sharper edge profile.

measured data. Both effects should reduce the achievable resolution in the reconstructed volumes.

Fourier ring correlations

To quantify the deterioration in reconstruction quality, we again split each of the horizontally undersampled data sets into two halves. To keep the horizontal sampling in the two halves equal, we split the data sets by alternating scan grid lines. The two halves of each data set were then reconstructed separately using the CPT algorithm. The resulting volumes were then compared using the Fourier shell correlation, exactly as described above.

The resulting resolution estimates are presented in Fig. S5. The expected trend of increased step width resulting in a deteriorated resolution estimate is confirmed. In Fig. S6 the estimated resolution is plotted against the horizontal step size.

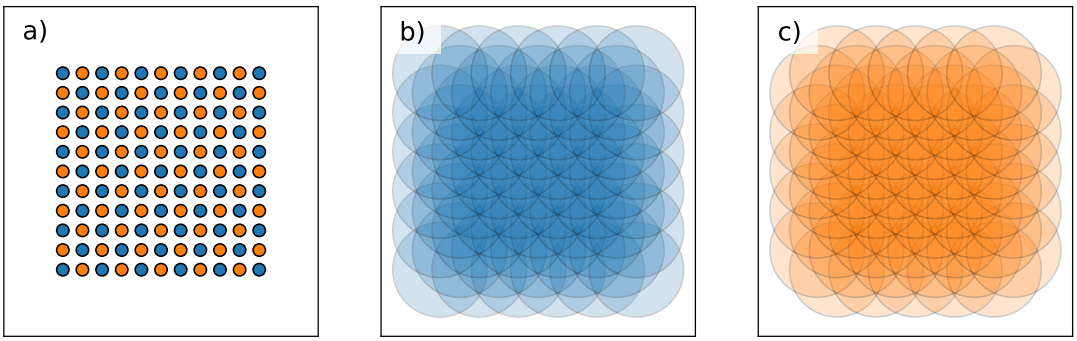

Fig. S2. a) shows the separation of the 11 × 11 diffraction patterns for each recorded angle into two halves (orange and blue) according to their position. This separation alternated between consecutive angles. b) and c) show the relative overlap between the different scan positions in the halved datasets.

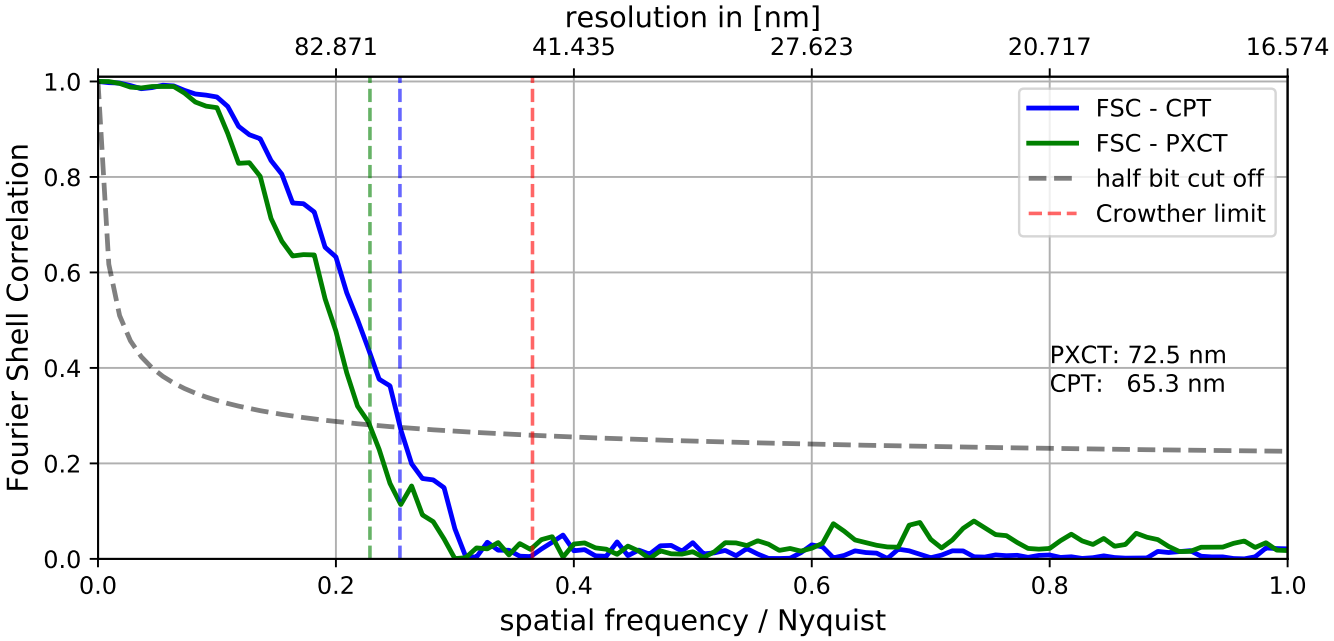

Fig. S3. Resolution estimation by Fourier shell correlation (FSC) computed by splitting the dataset in two halves, assigning for each projection the diffraction patterns alternately to one or the other halve. According to the FSC resolution estimate, the CPT reconstruction yields slightly higher resolution than PXCT.

REFERENCES

1. A. G. Machoke, A. M. Beltrán, A. Inayat, B. Winter, T. Weissenberger, N. Kruse, R. Güttel, E. Spiecker, and W. Schwieger, "Micro/macroporous system: Mfi-type zeolite crystals with embedded macropores," Adv. Mater. **27**, 1066–1070 (2015).
2. T. Weissenberger, B. Reiprich, A. G. F. Machoke, K. Klühspies, J. Bauer, R. Dotzel, J. L. Casci, and W. Schwieger, "Hierarchical mfi type zeolites with intracrystalline macropores: the effect of the macropore size on the deactivation behaviour in the mto reaction," Catal. Sci. Technol. **9**, 3259–3269 (2019).
3. D. Gürsoy, "Direct coupling of tomography and ptychography," Opt. Lett. **42**, 3169–3172 (2017).
4. A. M. Maiden and J. M. Rodenburg, "An improved ptychographical phase retrieval algorithm for diffractive imaging," Ultramicroscopy. **109**, 1256 – 1262 (2009).
5. M. van Heel and M. Schatz, "Fourier shell correlation threshold criteria," J. Struct. Biol. **151**, 250 – 262 (2005).
6. P. A. Penczek, "Chapter three - resolution measures in molecular electron microscopy," in *Cryo-EM, Part B: 3-D Reconstruction*, , vol. 482 of *Methods in Enzymology* G. J. Jensen, ed. (Academic Press, 2010), pp. 73 – 100.

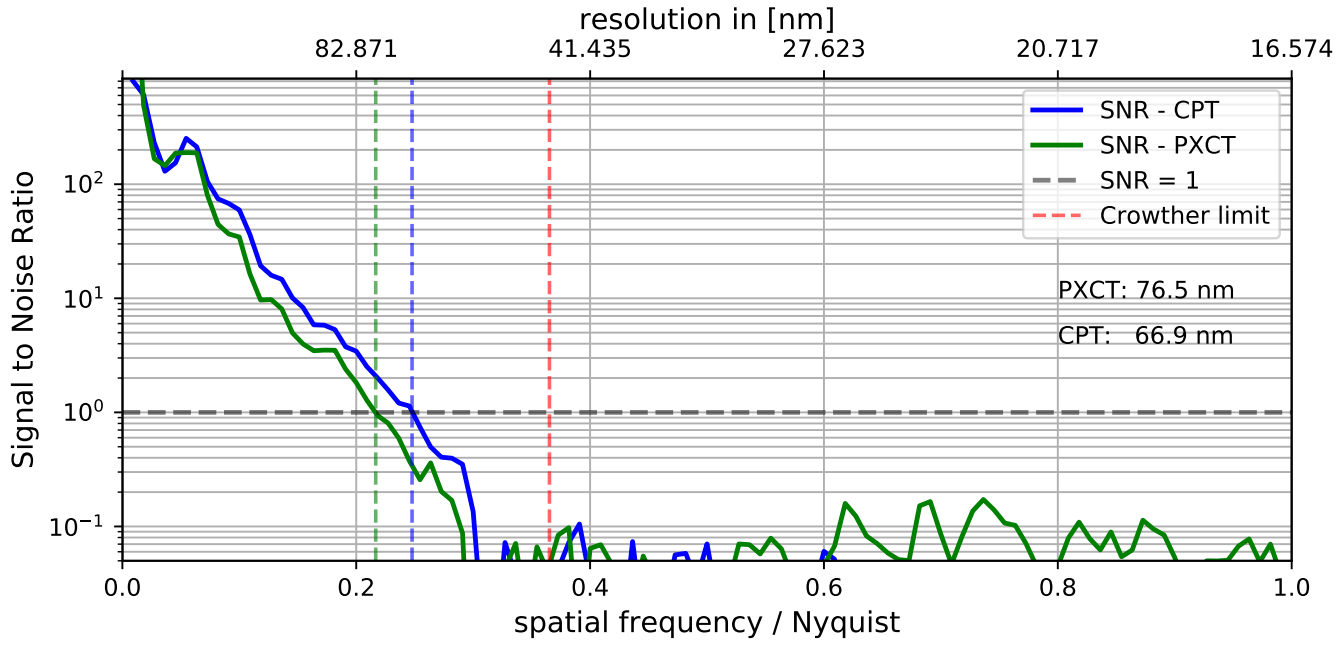

Fig. S4. Resolution estimation using the spectral signal to noise ratio computed using all 90 projections, but two complementary halves of all the diffraction patterns per projection angle. According to the spectral-signal-to-noise-ratio criterion, the CPT reconstruction shows slightly higher spatial resolution than PXCT.

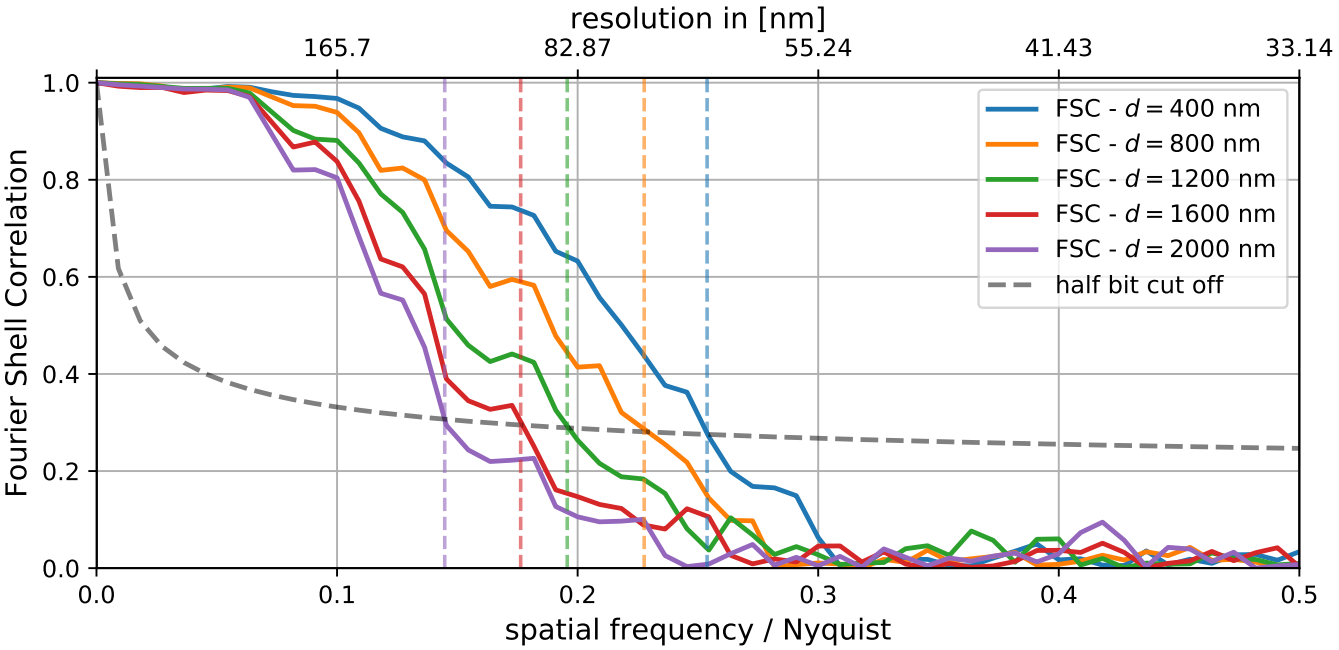

Fig. S5. Fourier shell correlations of the undersampled CPT reconstructions shown in Fig. **??** f-j) only using every nth diffraction pattern in the horizontal direction ($n = 1, \ldots, 5$). The estimated resolutions are: 65.3 nm ($n = 1$, $d = 400$ nm, blue), 72.8 nm ($n = 2$, $d = 800$ nm, orange), 84.7 nm ($n = 3$, $d = 1200$ nm, green), 94.0 nm ($n = 4$, $d = 1600$ nm, red), 114.5 nm ($n = 5$, $d = 2000$ nm, violet).

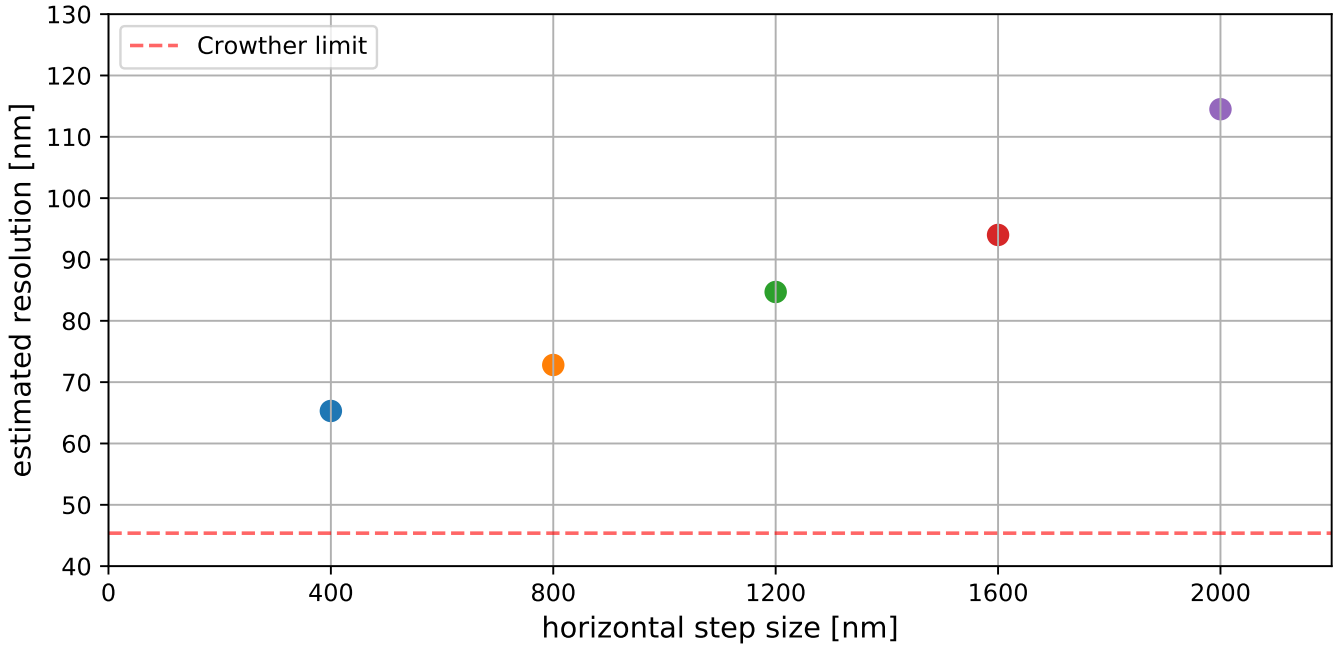

Fig. S6. Horizontal step sizes of the undersampled datasets plotted against the resulting estimated resolutions.